*Rev. Roum. Sci. Techn.– Électrotechn. et Énerg.*
Vol. **70**, *2*, pp. 159–164, Bucarest, 2025



# ESTIMATION OF THE FLUX LINKAGE OF PERMANENT MAGNET SYNCHRONOUS MOTOR USING KALMAN FILTER

PRITISH KUMAR GHOSH[1], ALOK KUMAR SHRIVASTA[2], RAJU BASAK[3]

**Keywords: Permanent magnet synchronous motor (PMSM); Space vector pulse width modulation (SVPWM); Kalman filter; Flux linkage; Finite element method (FEM).**

**The actual flux linkage value on the rotor side of a permanent magnet synchronous motor (PMSM) determines the motor's field control performance. The rotor side's flux linkage is a constant parameter for half of the full-order observer and stator flux estimate. However, realistically speaking, flux linkage can vary over a wide range. A new set of variables is established for internal permanent magnet synchronous motors, or IPMSMs. A third-order Kalman filter is developed by considering a set of additional variables and the state variables of the rotor flux linkage. Using $L_d = L_q$, the flux linkage of the rotor side for a surface-mounted PMSM may be shown. The model is simulated using the finite element method (FEM) to evaluate the effectiveness of the proposed approach. The computed findings indicate the precision of the flux linkage on the rotor side.**

## 1. INTRODUCTION

Servomotors designed using permanent magnet synchronous motors (PMSMs) have gained extensive recognition in modern industrial and technological applications due to their superior efficiency, robust performance, and precise operational control. These motors have outperformed traditional counterparts by offering enhanced torque-to-weight ratios, reduced noise levels, and better power factor characteristics, making them ideal for robotics, automation, and high-speed rail transport applications. Researchers have proposed various methodologies to address the complexities associated with PMSM operations, ranging from empirical models to computational techniques. Electromagnetic (EM) field theoretical analysis has played a pivotal role in understanding and improving motor dynamics. Both one-dimensional and two-dimensional EM field frameworks have been employed to examine the distribution of air-gap flux density, which is critical for ensuring optimal motor performance under variable operating conditions [1,4]. Circuit model analogies and finite element analysis (FEA) further supplement these studies by providing simplified yet effective tools for analyzing motor parameters and estimating essential performance metrics such as thrust and torque [2,3]. Dynamic effects, particularly in linear induction motors (LIMs), present unique challenges, such as the reverse wave braking phenomenon, which diminishes thrust efficiency and increases braking intensity. As speed increases, these effects become more pronounced, necessitating the use of advanced modeling and optimization strategies [6–8]. Applying Maxwell's equations has been instrumental in quantifying these dynamic influences, especially for high-speed LIMs, where thrust degradation due to configuration parameters, such as pole pitch and electrical frequency, demands meticulous analysis and design refinement [5,23].

The advancement of control strategies has been fundamental in mitigating dynamic challenges and enhancing motor performance. Vector control techniques have revolutionized the precise manipulation of flux and torque in PMSMs, enabling improved operational stability and performance [9][26]. Energy management approaches, such as slip frequency control, have been introduced to optimize energy utilization without increasing the motor's power requirements, thereby improving overall efficiency [10,11]. Modern control theories, including adaptive and robust control mechanisms, have addressed parameter variability issues, thereby further stabilizing motor operations [16, 17,25]. The accurate estimation and monitoring of rotor flux linkage remain crucial for the reliability of permanent magnet synchronous motors (PMSMs). Traditional flux observers, which assume fixed parameters, often fall short in accounting for real-world variations caused by temperature fluctuations and magnetic saturation [18,20]. Researchers have integrated space vector modulation with advanced Kalman filtering techniques to overcome these limitations. A third-order Kalman filter, which dynamically adjusts to rotor flux linkage variations by incorporating state variables, has shown promise in improving monitoring accuracy and control precision [21,22]. For surface-mounted permanent magnet synchronous motors (SPMSMs), the alignment of inductances $L_{dL}$ and $L_{qL}$ within the Kalman filter framework allows for reliable flux linkage estimation, as validated by experimental and simulation studies. Moreover, mathematical modeling in synchronous reference frames has been pivotal in developing strategies to address transient dynamics and improve thrust efficiency in motors with intermittent acceleration. Experimental validations and simulations have consistently demonstrated the effectiveness of these control strategies, highlighting their potential for broader applications. The experimental and simulation results demonstrate the accuracy of the proposed Kalman filter for flux estimation and motor parameter estimation.

## 2. SPACE VECTOR PULSE WIDTH MODULATION (SVPWM) SCHEME

Space Vector Pulse Width Modulation (SV-PWM) is a modulation scheme shown in Fig.1 that is being utilized for a defined voltage vector to a 3ϕ electric PMSM [9–13]. The details of the operating schemes are explained as follows:

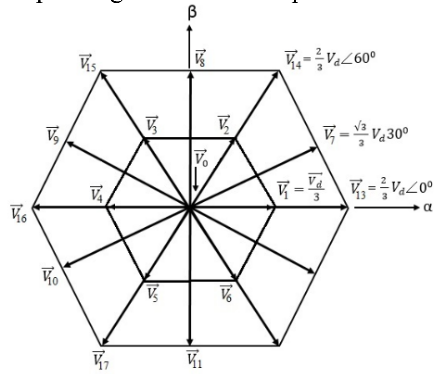


Fig. 1 – Three-phase sinusoidal system with rotating equivalent space vector.

[1] Training & Placement Officer, AIEM, WB, India. E-mail: aiemplacementcell@jisgroup.org
[2] Department of Electrical Engineering, JISCE, India. E-mail: alok.shrivastav@jiscollege.ac.in
[3] Department of Electrical Engineering, Techno India University, India. E-mail: raju.b@technoindiaeducation.com

DOI: 10.59277/RRST-EE.2025.2.1

In stage 1, the circle in Fig. 2 illustrates the three-phase voltages at variable angles, collectively forming a space vector with a fixed magnitude and angle. Stage 2 illustrates the significance of different switching states. The key objective in this section is the dotted lines present in Fig. 3. They control the voltages that cut the triangular wave [16,17]. The six stages of vector rotation in a three-phase system correspond to the sequential transitions of the space vector as it rotates through 360ºin the complex plane during a complete cycle. Each stage spans 60º and represents a specific phase relationship in the three-phase voltages or currents. In the first stage (0º–60º), the space vector lies between the dominant phases V1 and V2, with phase 3 contributing the least. In the second stage (60º–120º), the vector lies between V2 and V3, with V1 becoming the least significant contributor. The third stage (120º–180º) sees the vector aligning between V3 and V1, while V2 plays a minimal role. As the vector continues to rotate, the fourth stage (180º–240º) is dominated by the contributions of V3 and V2 (now reversed in polarity), while V1 contributes the least. In the fifth stage (240º–300º), the vector transitions to align with V2 and V1 (both with reversed polarity), and V3 becomes the smallest. Finally, in the sixth stage (300º–360º), the vector aligns between V1 and V3 (also reversed polarity) before completing its rotation and returning to its original position.

Figure 2 shows the highest value of both the circle and sector vector diagrams. The thin line inside the space vector depicts that these two desired space vectors give a complete vector sum. Figure 3 presents the zero vectors of $V_1$ to $V_6$. The winding angles inside the stator are designed at 1200 phase displacement. Since (+) ve and (-) ve voltage may appear in all windings, it is placed in an 1800 of phase shift. The control scheme with voltage conversion is illustrated in Fig. 4. The 3φ to 2φ transformation, along with the d-q axis and PI controller with a Kalman filter, are utilized correspondingly.

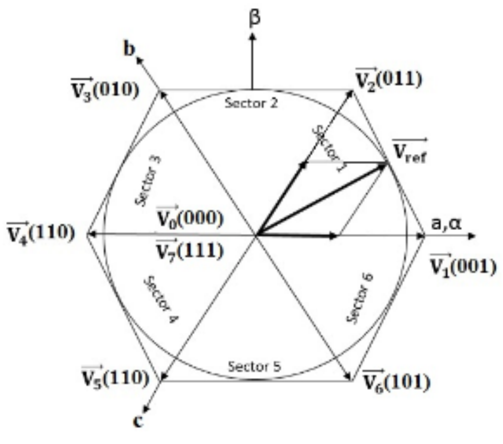


Fig. 2 – Second phase of rotation.

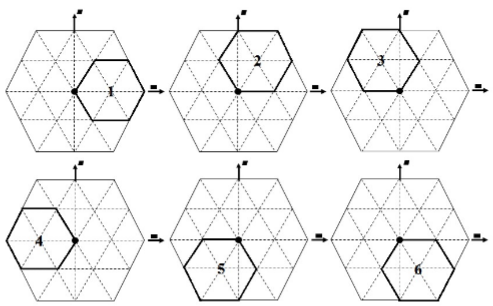


Fig.3 – Six stages of vector rotation in a three-phase supply.

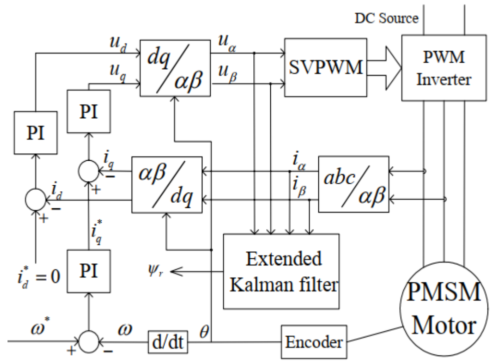


Fig. 4 – The block diagram of the simulation system.

## 3. KALMAN FILTER

The least-squares state estimation of the Kalman filter is added to extend its applications in dynamic systems where the parameters are not fixed [18]. The measurement of noise in recursive processing is its main application. The summary is described in this section. Let the state-space model for measurement be discrete, and the system of interest may be explained as:

$$x_{k+1} = Ax_k + Bu_k + \omega_k, \tag{1}$$

$$y_k = Hx_k + \mu_k, \tag{2}$$

where $\omega_k$ and $\mu_k$ are zero-average Gaussian errors with covariance $Q(t)$ and $R(t_k)$ correspondingly and are not dependent on the system's state. The system's disturbance and the model's efficacy are affected by the system's error, illustrating the noise in measurement [19,20]. The state vector $x(t_0)$ is a Gaussian random vector with an average value $x_0$ and covariance $p_0$. The input system vector is represented by $u(t)$. The cycle $xe_{klk}$ expresses the most favorable estimation produced by the filter $x(t)$. The best state and its covariance $p_{klk}$ are computed in two stages [21,24]. The first stage presents the efficacy of the forecast for the amount depending on the earlier measurement $xek_{-l|k-1}$ and reference input $\{U_{k-1|k-1}\}$, which is applied to the system for $t_{k-1}$ to $t_k$ period. A rectangular integration method is utilized in this paper, with the intention that the output of the forecasted stagusing4).

The other stage corrects the forecasted estimation of the state and its covariance value using a feedback correction technique that incorporates the actual use of estimated quantities. This is expressed by:

$$xe_{k|k} = xe_{k|k-1} + K_k\left(y_k - Hxe_{k|k-1}\right), \tag{5}$$

$$P_{k|k-1} = P_{k-1|k-1} + \left(A_{k-1}P_{k-1|k-1} + P_{k-1|k-1}A_{k-1}\right)T_c + Q_d, \tag{6}$$

where

$$K_k = P_{k|k-1}H'\left(HP_{k|k-1}H' + R\right)^{-1}. \tag{7}$$

## 4. MODELLING OF MOTOR

The PMSM is considered a non-salient, surface-mounted, salient-type interior permanent magnet synchronous motor. The interior PMSM is included in this section. However, surface PMSM is also considered in the conclusion. Under the suggested technique, the flux linkage is in the rotor side surface PMSM can also be viewed by replacing $L_d = L_q$. The equation of an α−β coordinate of salient type PMSM is represented by

$$\begin{bmatrix} V_\alpha \\ V_\beta \end{bmatrix} = \begin{bmatrix} R + pL_\alpha pL_{\alpha\beta} \\ pL_{\alpha\beta}R + pL_\beta \end{bmatrix} + \omega\psi_r \begin{bmatrix} -\sin\theta \\ \cos\theta \end{bmatrix}, \tag{8}$$

where

$$L_\alpha = L_\lambda + L_\delta \cos(2\theta_0),$$
$$L_\beta = L_\lambda - L_\delta \cos(2\theta_0),$$
$$L_{\alpha\beta} = L_\delta \sin(2\theta\mathrm{i}),$$
$$L_\lambda = \frac{(L_d+L_q)}{2},$$
$$L_\delta = \frac{(L_d-L_q)}{2}.$$

The inductance of rotating d & q coordinates individually. Also, the flux linkage of the rotor side is represented by $\psi_r$. Equation 8 must express a standard state space model, as eq. (1) shows.

$$\begin{bmatrix} V_\alpha \\ V_\beta \end{bmatrix} = R\begin{bmatrix} i_\alpha \\ i_\beta \end{bmatrix} + pL_\lambda \begin{bmatrix} i_\alpha \\ i_\beta \end{bmatrix} + pL_\delta \begin{bmatrix} \cos(2\theta_0) & \sin(2\theta_\mathrm{i}) \\ \sin(2\theta_\mathrm{i}) & \text{-} \cos(2\theta_0) \end{bmatrix} \begin{bmatrix} i_\alpha \\ i_\theta \end{bmatrix} + +\omega\psi_r \begin{bmatrix} -\sin\theta \\ \cos\theta \end{bmatrix}, \tag{9}$$

$$p\left(L_\lambda + L_\delta \begin{bmatrix} \cos(2\theta_0) & \sin(2\theta_i) \\ \sin(2\theta_\mathrm{i} - \cos 2\,\theta_0) & \end{bmatrix}\right)\begin{bmatrix} i_\alpha \\ i_\beta \end{bmatrix} = \begin{bmatrix} V_\alpha \\ V_\beta \end{bmatrix} - p\begin{bmatrix} i_\alpha \\ i_\beta \end{bmatrix} - \omega\psi_r \begin{bmatrix} -\sin\theta \\ \cos\theta \end{bmatrix}, \tag{10}$$

$$p\left(L_\lambda + L_\delta \begin{bmatrix} \cos(2\theta_0) & \sin(2\theta_i) \\ \sin(2\theta_i) & -\cos(2\theta_0) \end{bmatrix}\right)\begin{bmatrix} i_\alpha \\ i_\beta \end{bmatrix} = -\frac{R}{L_0} \tag{11}$$

$$\left(L_\lambda + L_\delta \begin{bmatrix} \cos(2\theta_0) & \sin(2\theta_i) \\ \sin(2\theta_i) & -\cos(2\theta_0) \end{bmatrix}\right)\begin{bmatrix} i_\alpha \\ i_\beta \end{bmatrix} + \begin{bmatrix} V_\alpha \\ V_\beta \end{bmatrix} - \omega\psi_r \begin{bmatrix} -\sin\theta \\ \cos\theta \end{bmatrix} + R\frac{L_\delta}{L_\lambda}\begin{bmatrix} \cos(2\theta_0) & \sin(2\theta_i) \\ \sin(2\theta_i) & -\cos(2\theta_0) \end{bmatrix}\begin{bmatrix} i_\alpha \\ i_\beta \end{bmatrix}. \tag{12}$$

In the same way, a set of new variables is expressed as

$$\begin{bmatrix} \xi_\alpha \\ \xi_\beta \end{bmatrix} = \left(L_\lambda + L_\delta \begin{bmatrix} \cos(2\theta_0) & \sin(2\theta_i) \\ \sin(2\theta_i) & -\cos(2\theta_0) \end{bmatrix}\right)\begin{bmatrix} i_\alpha \\ i_\beta \end{bmatrix}. \tag{13}$$

By using eq. (13) and (12) yields

$$p\begin{bmatrix} \xi_\alpha \\ \xi_\beta \end{bmatrix} = -\frac{R}{L_\lambda}\begin{bmatrix} \xi_\alpha \\ \xi_\beta \end{bmatrix} + \begin{bmatrix} V_\alpha \\ V_\beta \end{bmatrix} - \omega\psi_r \begin{bmatrix} -\sin\theta \\ \cos\theta \end{bmatrix} + +R\frac{L_1}{L_0}\left(L_\lambda + L_\delta \begin{bmatrix} \cos(2\theta_0) & \sin(2\theta_i) \\ \sin(2\theta_i) & -\cos(2\theta_0) \end{bmatrix}\right)\begin{bmatrix} i_\alpha \\ i_\beta \end{bmatrix}. \tag{14}$$

It can be considered a state variable to monitor the rotor side's flux linkage. Since the flux linkage may not alter quickly, the flux linkage of the rotor side is fixed to zero

$$\frac{\mathrm{d}\psi_r}{dt} = 0\,. \tag{15}$$

Further, a 3rd-order Kalman filter is designed for flux linkage in the rotor as state, input, and output form of vectors given by

$$x = \left[\xi_\alpha \xi_\beta \psi_r\right], \tag{16}$$

$$u = \begin{bmatrix} v_\alpha + R\frac{L_\delta}{L_\lambda}(\cos(2\theta\cos\alpha) + \sin(2\theta\sin\beta)) \\ v_\beta + R\frac{L_\delta}{L_\lambda}(\sin(2\theta\sin\alpha) - \cos(2\theta\cos\beta)) \end{bmatrix}, \tag{17}$$

$$y = \begin{bmatrix} \xi_\alpha & \xi_\beta & \psi_r \end{bmatrix}. \tag{18}$$

The measurements of the system and output matrix are

$$\dot{x} = \begin{bmatrix} -\frac{R}{L_\lambda} & 0 & \omega\sin(\theta) \\ 0 & -\frac{R}{L_\lambda} & -\omega\cos(\theta) \\ 0 & 0 & -\frac{R}{L_\lambda} \end{bmatrix} x + \begin{bmatrix} 1 & 0 \\ 0 & 1 \\ 0 & 1 \end{bmatrix} u, \tag{19}$$

$$Y = \begin{bmatrix} 1 & 0 & 0 \\ 0 & 1 & 0 \\ 0 & 0 & 1 \end{bmatrix} x.$$

The position θ and speed ω of the motor are obtained from the motor's encoder. Figure 4 illustrates the contro,l structure for a PMSM using FOC designed for high-performance applications such as electric vehicles, robotics, and industrial automation. The system integrates speed and current control loops to ensure precise and efficient motor operation. A PWM inverter, driven by space vector pulse width modulation (SVPWM), converts DC input into a balanced three-phase AC supply for the motor. SVPWM optimizes DC voltage utilization, reduces harmonic distortion, and ensures smooth torque generation. The control system comprises the outer speed loop and the inner current loop. The speed loop compares the desired speed (ω∗) with the actual speed (ω) and adjusts the reference quadrature-axis current ($i_q$∗), which directly determines the motor torque. The current loop regulates the stator currents in the dq-reference frame, where the d-axis current ($i_d$) is set to zero for optimal efficiency. Proportional-integral (PI) controllers minimize errors and generate control voltages (uq) for SVPWM. An extended Kalman filter (EKF) enhances the system by estimating rotor position (θ), speed (ω), and flux ($\psi_r$) from current measurements, enabling sensorless control or improving encoder feedback accuracy. $\xi_\alpha$ and $\xi_\beta$ represent the α-axis and β-axis components of the stator flux linkage. This structure ensures high precision, dynamic response, and energy efficiency. It is ideal for applications requiring smooth torque, low vibration, and robust control, such as electric vehicles, robotic arms, and industrial drives.

Hence, the suggested system shows the linearity for both input and output of the system by selecting state variables as $[\zeta_\alpha \quad \zeta_\beta \quad \psi_\tau]$ and output of the system $[\zeta_\alpha \quad \zeta_\beta]$.

## 4. RESULTS AND DISCUSSION

The efficacy of the suggested observer for flux linkage on the rotor side is checked and performed in a MATLAB simulation. The parameter of the motor is presented in Table 1. The sampling period of current, speed, and Kalman filter is 200 µs. The values of $R_c$, $Q_d$ and $P_0$ are chosen as

$$R_c = \begin{bmatrix} 0.1 & 0 & 0 \\ 0 & 0.1 & 0 \\ 0 & 0 & 0.1 \end{bmatrix}, \tag{20}$$

$$Q_d = \begin{bmatrix} 0.1 & 0 & 0 \\ 0 & 0.1 & 0 \\ 0 & 0 & 0.2 \end{bmatrix}, \tag{21}$$

$$P_0 = \begin{bmatrix} 0.1 & 0 & 0 \\ 0 & 0.1 & 0 \\ 0 & 0 & 0.1 \end{bmatrix}. \tag{22}$$

The suggested observer is not sensitive to the preliminary state, and its value is fixed to zero. Figure 5 shows the estimated flux linkage of the rotor at the start with standard motor parameters. Figure 6 presents the estimated rotor inductance interpolation (simulation) during startup with 150 % standard stator resistance. The suggested observer has intense sensitivity to variations in motor parameters.

*Table 1*

Simulation parameters.

| Sl. No. | Parameters | Values |
|---|---|---|
| 1 | Voltage | 230 V |
| 2 | No. of poles (P) | 6 |
| 3 | Inductance of d-axis, $L_d$ | 55 mH |
| 4 | Inductance of q-axis, $L_q$ | 46 mH |
| 5 | Resistance of stator, $R_s$ | 2.1 Ω |
| 6 | Motor inertia, J | 0.00345 kgm$^2$ |
| 7 | Friction coefficient, B | 1.68. $10^{-3}$ Nm/rad/s |
| 8 | Magnetic flux constant φ | 0. 1256 Wb |

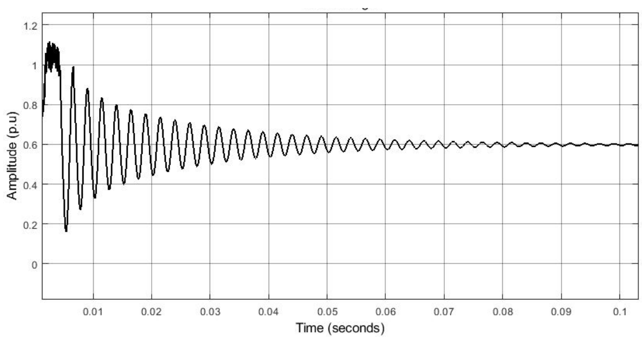


Fig. 5 – Estimated flux linan kage of the rotor with standard motor parameters.

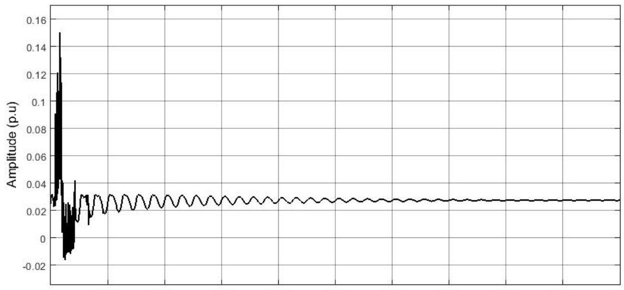


Fig. 6 – Estimated rotor inductance interpolation with nominal motor parameters.

The simulation results of three-phase voltage and current are shown in Figs. 7 and 8. The voltages are uniform and have almost negligible distortion. The output of SVPWM maintains linearity relative to the ideal output.

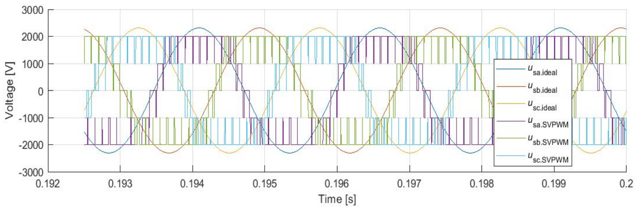


Fig. 7 – Three-phase voltage calculation under ideal and SVPWM techniques.

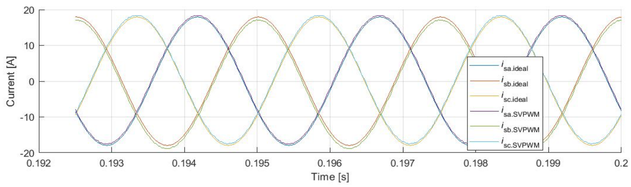


Fig. 8 – Estimated three-phase current under ideal and SVPWM scheme.

The electromagnetic power and torque shown in Figs. 9 and 10 are also calculated, and the simulation output shows the efficacy of the SVPWM technique. Figure 9 compares torque over time for a PMSM [24] under ideal and SVPWM control schemes. The x-axis shows time in seconds, while the y-axis displays torque in (N·m). Under Ideal conditions, the curve maintains a constant torque of approximately 145 N·m, indicating a stable performance. Conversely, the SVPWM curve exhibits a sinusoidal waveform, oscillating around the ideal torque level, highlighting the inherent torque ripple and dynamic characteristics introduced by the SVPWM control strategy.

Figure 10 compares power loss over time for two methods: PCu, ideal, and PCu, SVPWMP. The x-axis represents time ranging from 0.192 s to 0.2 s, and the y-axis represents power loss ranging from 550 W to 750 W. Moreover, the copper and iron losses are also computed under standard and SVPWM schemes, which depict that the implemented schemes give better outputs. The estimated iron loss of PMSM is shown in Fig. 11.

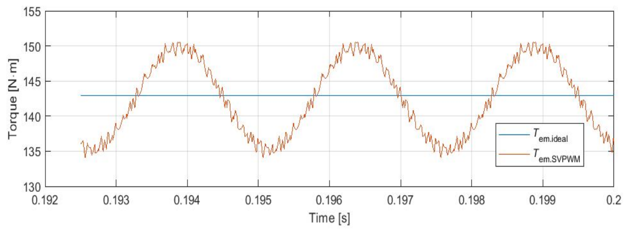


Fig. 9 – Estimated torque under ideal and SVPWM scheme.

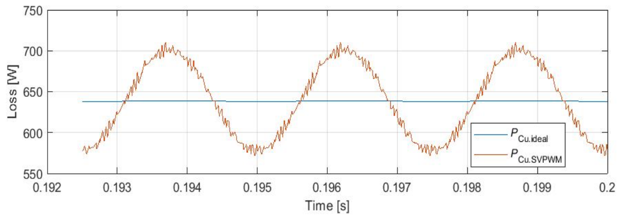


Fig. 10 – Estimated Copper loss under ideal and SVPWM scheme.

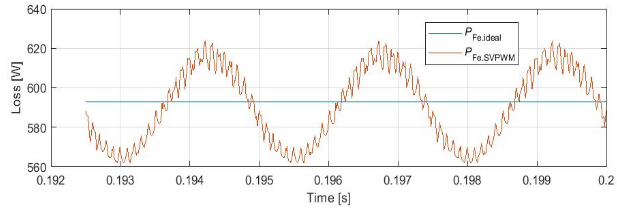


Fig. 11 – Estimated Iron loss under ideal and SVPWM scheme.

## 5. MODEL AUTHENTICATION BY FEM

To justify the above conclusions, the FEM was used. Initially, the frequency of slips related to the highest thrust outcomes marked by the machine is denoted as the standard slip frequency, which can be written as:

$$\omega_{s\_Fmax} = \frac{R_r}{L_m(t)+L_{lr}}. \tag{24}$$

In compliance with eq. (24), the standard slip frequency rises since the excitation level of inductance reduces because of its dynamic effect. To achieve the highest motor output at various speeds, FEM-based models with multiple speeds were developed in MATLAB and operated at variable frequencies, as shown in Fig. 12 (*i.e.*, 25 m/s). The graph presents multiple thrust profiles corresponding to different speed and frequency combinations, with the red curve emphasizing the representative or averaged response. The gradual attenuation of oscillations during the transient phase indicates the presence of effective damping mechanisms within the system. The steady-state values for thrust provide critical insights into system efficiency and stability, facilitating optimization for desired performance. The finite element-based simulation effectively models these dynamic behaviors, offering a detailed analysis of thrust characteristics under variable operational conditions.

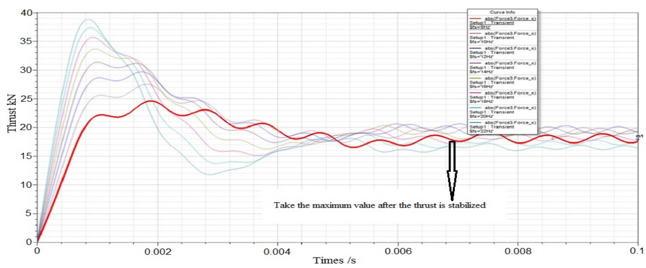


Fig. 12 – The FEM thrust outcomes at 25 m/s.

The simulated results are depicted in Fig. 13. T, acceleration waveform can be standardized with the highest value at 55 m/s, which is taken as a reference in the simulation. The outcome of the position controller is known as controlled acceleration. The waveform of velocity and position are obtained by measuring and computing the position sensor. The measured acceleration, position, and speed test outcomes can affect the motor's efficiency. The highest coincidence among the outcomes and preferred external ring waveform is the superior proficiency of the thrust control.

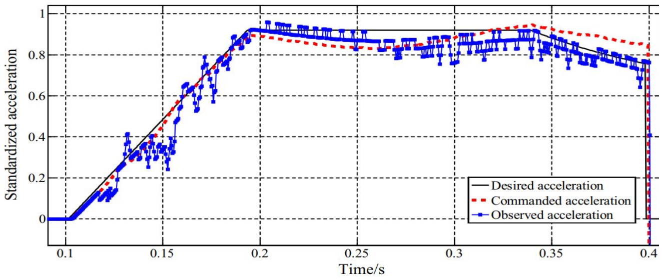


Figs. 13(a) – Simulated results of FEM.

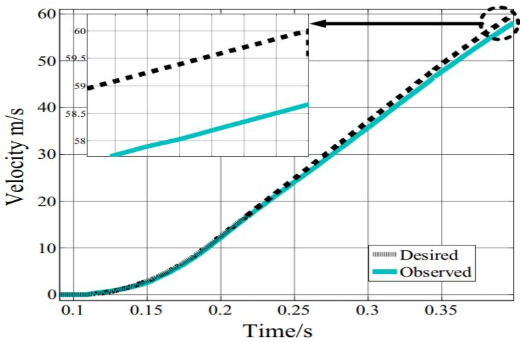


Figs. 13(b) – Simulated results of FEM.

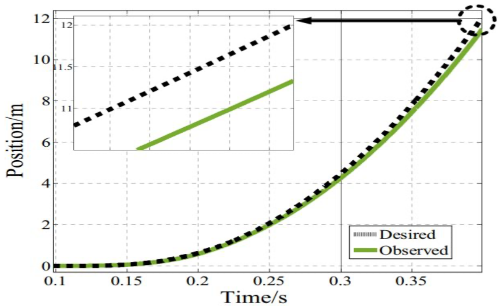


Figs. 13(c) – Simulated results of FEM.

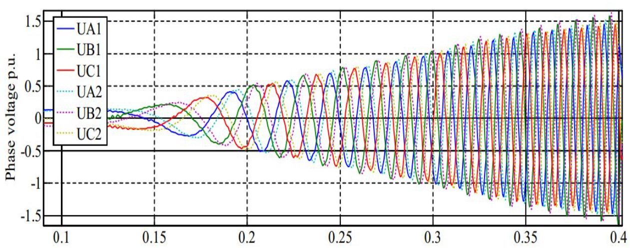


Fig. 13(d) – Simulated results of FEM.

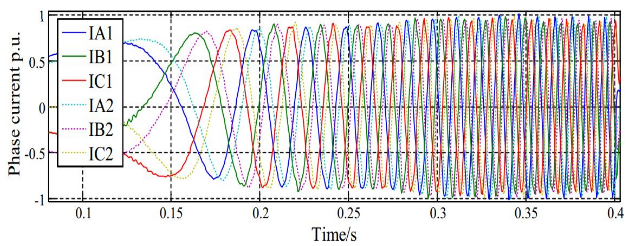


Figs. 13(e) – Simulated results of FEM.

The reductions of a model can be verified at various speeds, and the highest thrust can be achieved by comparing with the outcomes of FEM modeling and numerical computation obtained by an equivalent network model. The comparison of FEM outcomes with reference value and Kalman filter (Method 2) was presented in Fig. 14 without considering the outward leakage of inductance.

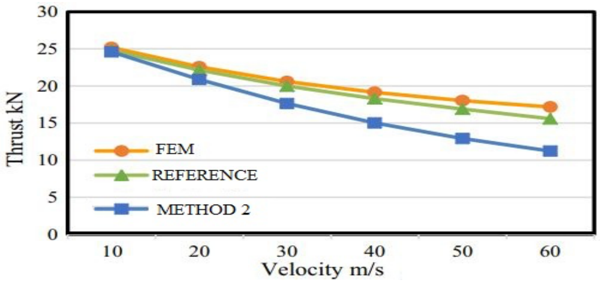


Fig. 14 – Comparison of two methods.

## 6. **CONCLUSION**

This paper suggests a Kalman filter-based observer for flux linkage on the rotor side. The mathematical modeling of IPMSM is rewritten for α-β coordinate. After presenting an original set of variables with zero linkage of rotor flux, a 3rd order Kalman filter is designed. Moreover, by replacing $L_d = L_q$ in SPMSM, the rotor flux linkage can also be observed. Additionally, the simulation model tested by FEM, considering each pattern with one switch start and end, begins and ends with a zero vector. This significantly minimizes harmonics and protects against torque fluctuations and overheating. The simulation results demonstrate that the proposed observer accurately estimates the flux linkage of the rotor and is unaffected by variations in motor parameters.

## CREDIT AUTHORSHIP CONTRIBUTION STATEMENT

Pritish Kumar Ghosh: conceptualization, methodology, writing – original draft.
Alok Kumar Shrivastav: data curation, software, validation.
Raju Basak: formal analysis, supervision, writing – review, and editing.

*Received on 19 May 2024*

## REFERENCES

1. A. Mora, J.J. Orellana, R. Cardenas, *Model predictive torque control for torque ripple compensation in variable-speed PMSMs*, IEEE Trans. Ind. Electron., **63**, *7*, pp. 4584–4592 (2016).
2. T. Nguyen, M.S. Rafaq, H.H. Choi, J.W. Jung, *A model reference adaptive control-based speed controller for a surface-mounted permanent magnet synchronous motor drive*, IEEE Trans. Ind. Electron., **65**, *12*, pp. 9399–9409 (2018).
3. D.K. Hong, J.Y. Lee, B.C. Woo, D.-H. Park, B.U. Nam, *Investigating a direct-drive PM type synchronous machine for turret application using optimization*, IEEE Trans. Magn., **48**, *11*, pp. 4491-4494 (2012).
4. E.K. Kim, J. Kim, H.T. Nguyen, H.H. Choi, J.W. Jung, *Compensation of parameter uncertainty using an adaptive sliding mode control strategy for an interior permanent magnet synchronous motor drive*, IEEE Access, **7**, pp. 11913–11923 (2019).
5. G. Hong, T. Wei, X. Ding, *Multi-objective optimal design of permanent magnet synchronous motor for high efficiency and high dynamic performance*, IEEE Access, **6**, pp. 23568–23581 (2018).
6. G. Foo, S. Sayeef, M.F. Rahman, *Low-speed and standstill operation of a sensorless direct torque and flux controlled IPM synchronous motor drive*, IEEE Trans. Energy Conversion, **25**, *1*, pp. 25–33 (2010).
7. H. Sira-Ramirez, J. Linares-Flores, C. Garcia-Rodriguez, M.A. Contreras-Ordaz, *On the control of the permanent magnet*

*synchronous motor: An active disturbance rejection control approach*, IEEE Trans. Control Syst. Technol., 22, 5, pp. 2056–2063 (2014).

8. W. Hu, C. Ruan, H. Nan, D. Sun, *Simplified modulation scheme for open-end winding PMSM system with common DC bus under open-phase fault based on circulating current suppression*, IEEE Trans. Power Electron., **35**, *1*, pp. 10–14 (2020).
9. J.L. Flores, C.G. Rodriguez, H.S. Ramirez, O.D.R. Cardenas, *Robust backstepping tracking controller for low-speed PMSM positioning system: Design, analysis, and implementation*, IEEE Trans. Ind. Informat., **11**, *5*, pp. 1130–1141 (2015).
10. J. Shi, F. Chai, X. Li, S. Cheng, *Study of the number of slots/pole combinations for low speed high torque permanent magnet synchronous motors*, Proc. Int. Conf. Electr. Mach. Syst., pp. 1–3, (2011).
11. K. Xiong, C.L. Wei, L.D. Liu, *Robust extended Kalman filtering for nonlinear system with stochastic uncertainties*, IEEE Trans on Systems, Man, and Cybernetics—Part A: Systems and Humans, **40**, *2*, pp. 399-405 (2010).
12. L. Castellini, M. Carmignano, M. d'Andrea, M. Villani, *Brushless PM actuator for metal bending machine*, Proc. 39th Annu. Conf. IEEE Ind. Electron. Soc. (IECON), pp. 2644–2649 (2013).
13. Q. Fei, Y. Deng, H. Li, J. Liu, M. Shao, *Speed ripple minimization of permanent magnet synchronous motor based on model predictive and iterative learning controls*, IEEE Access, **7**, pp. 31791–31800, (2019).
14. S. Wu, J. Zhang, *A robust adaptive control for permanent magnet synchronous motor subject to parameter uncertainties and input saturations*, J. Elect. Eng. Technol., **13**, *5*, pp. 2125–2133 (2018).
15. S.U. Chung, S.H. Moon, D.J. Kim, J.M. Kim, *Development of a 20–pole–24–slot SPMSM with consequent pole rotor for in-wheel direct drive*, IEEE Trans. Ind. Electron., **63**, *1*, pp. 302-309 (2016).
16. W. Sen, Z. Bingyi, F. Guihong, *Research of low-speed and direct-drive PMSM for new oil drilling mud pump*, Proc. Int. Conf. Electr. Mach. Syst., pp. 1–5, (2011).
17. W.H. Chen, J. Yang, L. Guo, S. Li, *Disturbance-observer-based control and related methods—An overview*, IEEE Trans. Ind. Electron., 63, 2, pp. 1083–1095, (2016).
18. X. Ge, Z. Q. Zhu, J. Li, J. Chen, *A spoke-type IPM machine with novel alternate airspace barriers and reduction of unipolar leakage flux by step-staggered rotor*, IEEE Trans. Ind. Appl., **52**, *6*, pp. 4789–4797 (2016).
19. H. Zhan, Z. Zhu, M. Odavic, *Analysis and suppression of zero sequence circulating current in open winding PMSM drives with common DC bus*, IEEE Trans. Ind., **53**, *4*, pp. 3609–3620 (2017).
20. B. Zhu, C. Tan, M. Farshadnia, *Postfault zero-sequence current injection for open-circuit diode/switch failure in open-end winding PMSM machines*, IEEE Trans. Ind. Electron., **66**, *7*, pp. 5124–5132 (2019).
21. Z. Xu, M.F. Rahman, *Comparison of a sliding observer and a Kalman filter for direct-torque-controlled IPM synchronous motor drives*, IEEE Trans. Industrial Electronics, **59**, *11*, pp. 4179-4188 (2012).
22. B. Raju, P.A. Kumar, *Cost-effective design of three-phase induction motor: an optimization approach*, Rev. Roum. Sci. Techn. – Électrotechn. Et Énerg., **67**, *4*, pp. 461–466 (2022).
23. S. Medjmadj, D. Diallo, A. Arias, *Mechanical sensor fault-tolerant controller in PMSM drive: experimental evaluation of observers and signal injection for position estimation*", Rev. Roum. Sci. Techn. – Électrotechn. Et Énerg., **66**, *2*, pp. 77–83 (2021).
24. B. Mokhtari, *Enhancement Ripples of a direct torque control applied to a permanent magnet synchronous motor by using a four-level multicellular inverter and a new reduced switching table*, Rev. Roum. Sci. Techn. – Électrotechn. Et Énerg., **69**, *2*, pp. 207–212 (2024).
25. N. Ali, A. W. Alam, M. Pervaiz, J. Iqbal, *Nonlinear adaptive backstepping control of permanent magnet synchronous motor*, Rev. Roum. Sci. Techn. – Électrotechn. Et Énerg., **66**, *1*, pp. 15–20 (2021).
26. A. Boulayoune, A. Oubelaid, A. Chibah, *Comparative study of inner and outer rotor flux reversal permanent magnet machine for direct drive wind turbine*, Rev. Roum. Sci. Techn. – Électrotechn. Et Énerg., **69,** *2*, pp. 123–128 (2024).